

Joint estimation of balanced motions and internal tides from future wide-swath altimetry

Florian Le Guillou¹, Noël Lahaye², Clément Ubelmann³, Sammy Metref¹, Emmanuel
Cosme¹, Aurélien Ponte⁴, Julien Le Sommer¹, Eric Blayo⁵, Arthur Vidard⁵

¹Univ. Grenoble Alpes, CNRS, IRD, Grenoble INP, IGE; Grenoble, France

²Inria & IRMAR, campus universitaire de Beaulieu, Rennes, France

³Ocean Next, Grenoble, France

⁴Univ. Brest, CNRS, IRD, Ifremer, Laboratoire d’Océanographie Physique et Spatiale (LOPS), IUEM, Brest, France

⁵Univ. Grenoble Alpes, CNRS, INRIA, Grenoble INP, LJK; Grenoble, France

Key Points:

- We present a dynamical method that estimates and separates balanced motions (BM) and internal tides (IT) from sea surface height data.
- The method uses iteratively two data assimilation techniques, each specific to the estimation of one component (BM or IT).
- Although idealized, this study shows encouraging results for the disentanglement of BM and IT signature on future SWOT data.

Abstract

The future Surface Water and Ocean Topography (SWOT) mission will soon provide Sea Surface Height (SSH) measurements resolving scales of a few tens of kilometers. Over a large fraction of the globe, the SSH signal at these scales is essentially a superposition of a component due to balanced motions (BM) and another component due to internal tides (IT). Several oceanographic applications require the separation of these components and their mapping on regular grids. For that purpose, the paper introduces an alternating minimization algorithm that iteratively implements two data assimilation techniques, each specific to the mapping of one component: a quasi-geostrophic model with Back-and-Forth Nudging for BM, and a linear shallow-water model with 4-Dimensional Variational (4DVar) assimilation for IT. The algorithm is tested with Observation System Simulation Experiments (OSSE) where the truth is provided by a primitive-equation ocean model in an idealized configuration simulating a turbulent jet and a mode-one IT. The algorithm reconstructs almost 80% of the variance of BM and IT, the remaining 20% being mostly due to dynamics that cannot be described by the simple models used. Importantly, in addition to the reconstruction of stationary IT, the amplitude and phase of nonstationary IT are reconstructed. Although idealized, this study represents a step forward towards the disentanglement of BM and IT signals from real SWOT data.

Plain Language Summary

The future Surface Water and Ocean Topography (SWOT) mission will soon provide Sea Surface Height (SSH) images with pixels of 2 km, informing about ocean motions at scales of a few tens of kilometers. At these scales, SSH variations are essentially due to the superposition of slow, balanced motions primarily driven by Earth rotation, and fast, propagating motions due to internal waves mainly generated by interactions between bathymetry and tidal water displacements. Several oceanographic applications require the separation of these two SSH components and their mapping on regular grids. This paper presents an original method to achieve this separation, based on data assimilation approaches and simple dynamical models. Experiments with synthetic SWOT observations, simulated from an ocean circulation model with detailed physics, show the efficiency of the method.

1 Introduction

For more than 25 years, altimetry has allowed the study of near-global sea surface height (SSH) at scales longer than 150 km and drastically transformed our understanding of mesoscale processes in the oceans. In particular, altimetry has given access to the upper-ocean circulation dynamics through geostrophy and revealed that most kinetic energy in the world ocean is contained in mesoscale eddies with wavelengths between 100 km and 300 km (Wunsch & Ferrari, 2004). But the scales resolved by nadir (along-track) altimetry are limited by the 100-300 km spacing between satellite ground tracks. Even by merging several nadir measurements (Taburet et al., 2019), the space time resolution of the resulting 2D SSH maps does not allow to conveniently characterize and study small mesoscale (<150km) motions (Ballarotta et al., 2019; Amores et al., 2018).

With wide-swath radar interferometry, the future SWOT mission (Morrow et al., 2019) will provide SSH observations over a 120km-wide swath with a near-global coverage, resolving spatial scales down to 15-30km depending on the sea state (Fu & Uebelmann, 2014). Recent studies, based on numerical models, have highlighted the impacts of short-mesoscale and submesoscale processes on ocean dynamics. Submesoscale motions have been found to trigger a large part of vertical motions (McWilliams, 2016; Klein & Lapeyre, 2009) that drive the exchanges of heat, carbon and nutrients between the ocean surface and subsurface. Small mesoscale processes also provide kinetic energy to larger scales through an inverse cascade (Ajayi et al., 2019; Capet et al., 2016), hence impacting the mesoscale dynamics. The SWOT mission rep-

resents a unique opportunity to validate our present-day understanding of submesoscale motions and their role in the oceanic processes in a broad sense.

At the scales measured by SWOT, some SSH variations due to internal tide (IT) may become comparable to those due to the short mesoscale balanced motions (BM; Qiu et al., 2018). IT, producing high frequency sea level fluctuations at scales around 200 km and below, are internal gravity waves generated when the barotropic tidal flow encounters variations of topography (Garrett & Kunze, 2007). Although the generation processes of IT are well understood, the dissipation processes (that greatly influence the ocean's energy budget) remain barely known. Recent studies emphasize that IT and BM interact in a complex way (Kelly & Lermusiaux, 2016), with BM scattering and refracting IT (Dunphy et al., 2017). These complex interactions are thought to strongly modify local mixing but need to be validated with observations. SWOT capacity to observe even a part of IT SSH signal will help to better understand these interactions and the processes related to ocean mixing and dissipation.

The accurate characterization of both IT and BM from SWOT, in the small mesoscale spectrum where their signatures overlap, will require scientific and technological developments for the processing of observations. The first challenge concerns the design of gridded products. For BM, the main objective is to increase the space-time resolution of the present-day SSH maps using SWOT. The mismatch between the (high) spatial and (low) temporal sampling of SWOT fosters the development of innovative inversion techniques, which typically include dynamical constraints (Ubelmann et al., 2015). For IT, the main objective is to map the incoherent part of the signal, i.e. the part due to waves which characteristics have been altered by interactions with BM and stratification variations. This is further developed in the next paragraph. The second challenge consists in the separation of IT and BM components from SWOT to make the differentiated gridded products possible. Both components are driven by different dynamics, and separation is needed to properly estimate quantities associated to each (e.g. surface currents for tracer advection, or energy dissipation due to waves). Separation is also made difficult by geographical and seasonal variations in the spatial scales and the relative strength of IT and BM (Qiu et al., 2018).

Disentangling the contribution of BM and IT on SSH is still an unsolved challenge. Due to its partial sampling in space and time, altimetry does not capture the fast SSH pulsation due to IT. Stationary IT (which are phase-locked to the astronomical forcing) can be mapped by harmonic analysis of long time series (>10 years) of conventional nadir altimetry data (Ray & Zaron, 2015). IT become non stationary when interacting with BM (Dunphy et al., 2017; Ponte & Klein, 2015) and/or being modulated by the stratification (Ray & Zaron, 2011). The phase and amplitude modulations of the IT field can evolve on time scales between 5 and 20 days, what make their predictability nearly impossible with conventional satellite altimetry (Nash et al., 2012; Haren et al., 2004). Recent studies (Zaron, 2017; Nelson et al., 2019) suggest that nonstationarity represents half of the total IT variance on average. SWOT will considerably increase the SSH measurement density and open the way to predicting nonstationary IT. In the context of SWOT development, the BM-IT separation problem has been addressed with various approaches. Torres et al. (2019) make use of a spatial scale threshold above which BM dominate and below which IT dominate. This spectral technique is less effective when the common spatial scale interval extends too much, what is particularly the case in winter due to the emergence of small vortices (< 50 km) associated with mixed layer instabilities (Ajayi et al., 2020). Ponte et al. (2017) and Gonzalez-Haro et al. (2019) explore multi-sensor approaches with altimetry and sea surface temperature observations, motivated by the fact that BM and IT have distinct footprints on both fields.

In this paper, we propose to simultaneously and dynamically map and separate SSH components of BM and IT from 2D altimetric observations, distributed in time, as SWOT data will be. The proposed approach, illustrated on Figure 1, implements an alternating minimization algorithm that iteratively calls two mapping techniques, each one specific to the estimation of a component (BM or IT). At each iteration, the observations used to map one component is made of the difference between the full observation and the previous estimation of the other

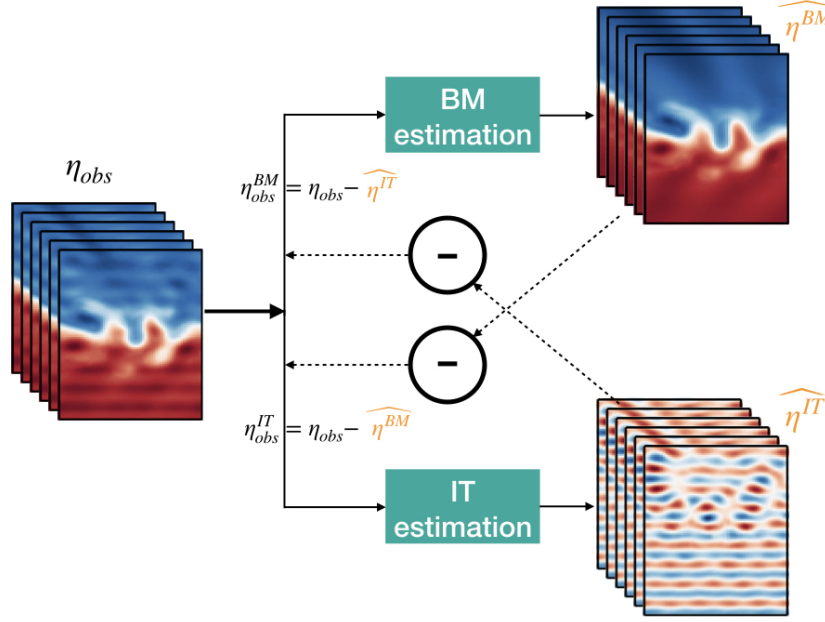


Figure 1. The joint estimation algorithm alternates BM estimations and IT estimations with observations recursively corrected from the other component. The algorithm is formalized and described in Section 4.

component. Both mapping techniques are based on data assimilation. BM are reconstructed with a Quasi-Geostrophic (QG) model assimilating observations with a Back-and-Forth Nudging (BFN) technique (Auroux & Blum, 2008). The algorithm is called BFN-QG hereafter. IT are reconstructed with a Shallow-Water model (SW) assimilating observations with a 4DVar technique (DIMET & TALAGRAND, 1986). The algorithm is called 4DVar-SW hereafter. The joint estimation algorithm is tested with observing system simulation experiments (OSSE). The true state of the ocean (illustrated on Figure 2) is provided by a primitive-equation regional model, ROMS, in an idealized configuration that simulates the propagation of a mode-one IT through a turbulent mesoscale zonal jet (Ponte et al., 2017; Dunphy et al., 2017).

The paper is structured as follows: Sections 2 and 3 present the data assimilation algorithms reconstructing BM and IT, respectively; Section 4 formalizes and describes the general joint estimation approach that implements both assimilation algorithms; The experimental set-up is presented in Section 5 and the results are discussed in Section 6; Conclusions and perspectives are drawn in section 7.

2 Mapping the balanced motions: BFN-QG algorithm.

The mapping technique for BM is presented in detail in Guillou et al. (2021). It is based on a quasigeostrophic (QG) model and a data assimilation method called the Back and Forth Nudging (Auroux & Blum, 2008), and referred to as BFN-QG. The dynamical model is a 1.5-layer QG model (Ubelmann et al., 2015). Forcing and mixing terms are omitted, resulting in the simplified QG equations:

$$\frac{\partial q}{\partial t} + J(\psi, q) = 0 \quad (1)$$

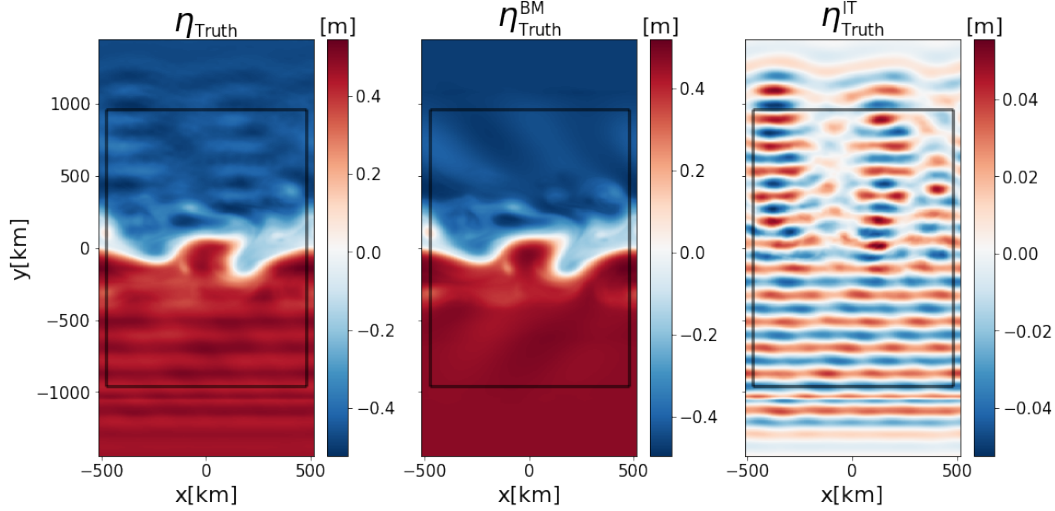


Figure 2. SSH snapshot of the simulated true state of the ocean (left), its BM component (middle) and its IT component (right). The black square represents the study domain in which the reconstructions are performed.

where J is the Jacobian operator and the streamfunction ψ is proportional to SSH η :

$$\psi = \frac{g}{f} \eta \quad (2)$$

with g the gravity constant, and f the Coriolis parameter. The PV is linked to the streamfunction by the elliptical equation:

$$q = \nabla^2 \psi - \frac{1}{L_R^2} \psi \quad (3)$$

where ∇^2 is the Laplace operator and L_R is the first baroclinic Rossby radius of deformation. Propagating SSH from time t_i to time t_{i+1} is a succession of elementary steps: (i) compute q_i from η_i with equations 2 and 3, (ii) propagate q_i with equation 1 to obtain q_{i+1} , (iii) invert equation 3 to retrieve ψ_{i+1} , then η_{i+1} .

The BFN technique is based on the Nudging method (Anthes, 1974), which consists of adding an extra term to the model prognostic equation (equation 1) to pull the model variable towards the observations. This term is proportional to the difference between the observations and the model variable. Here, the model variable is PV q and the observations are 2D SSH η_{obs} . Thanks to equations 2 and 3, a corresponding PV observation q_{obs} can be derived from η_{obs} and used to nudge Eq. 1 as:

$$\frac{\partial q}{\partial t} + J(\psi, q) - K(q_{\text{obs}} - q) = 0 \quad (4)$$

where K is a tunable coefficient controlling the strength of nudging. As explained in (Guillou et al., 2021), K must exhibit smooth variations in time to avoid the emergence of numerical instabilities and enhance the constraint of the observations on the model dynamics. A Gaussian kernel is used for K :

$$K[t] = \sum_{t_{\text{obs}}} K_0 e^{-\left(\frac{t-t_{\text{obs}}}{\tau}\right)^2} \quad (5)$$

where K_0 and τ are the nudging parameters and t_{obs} are the observation times.

Nudging is also performed backward in time, by adding a feedback term with a sign opposite to that of the forward nudging. Note that the backward integration of the model is possible because the model equation 1 is reversible in time.

The BFN is the combination of the forward nudging and the backward nudging over a sliding time window of length T_{BFN} . Over a specific time window $[t_i, t_i + T_{\text{BFN}}]$, the algorithm works as follows. The model state at time t_i is prescribed from the previous time window. The forward nudging is first computed from t_i to $t_i + T_{\text{BFN}}$. The final state at $t_i + T_{\text{BFN}}$ is then used as initial condition to run the backward nudging back to t_i . The result initializes the forward nudging, and so on until convergence. In a few iterations, the model converges towards a trajectory that both fits the observations and complies with the QG dynamics. The process can then be carried out in the next time window.

3 Mapping the internal tide signal: 4Dvar-SW algorithm.

3.1 Dynamical model

The dynamical model used to simulate the surface propagation of IT motions is a linear shallow water (SW) model. This model represents the first baroclinic mode dynamics assumed to capture the largest part of the IT signal (Ray & Zaron, 2016). The equations are (Gill, 1982):

$$\frac{\partial u}{\partial t} - fv = -g \frac{\partial \eta}{\partial x}, \quad (6a)$$

$$\frac{\partial v}{\partial t} + fu = -g \frac{\partial \eta}{\partial y}, \quad (6b)$$

$$\frac{\partial \eta}{\partial t} = -H_e \left(\frac{\partial u}{\partial x} + \frac{\partial v}{\partial y} \right), \quad (6c)$$

where (u, v) are the velocity components, η is the SSH, f is the Coriolis frequency, and H_e the equivalent depth that determines the baroclinic deformation radius (through the relation $R_d = \sqrt{gH_e}/f$). Equations 6 are discretized on a C-grid and a leap-frog time-stepping scheme (Sadourny, 1975). The domain is a square, land-free domain with a flat bottom and open boundaries. IT enter through the boundaries and are not generated within the domain.

After entering the domain, IT can be made incoherent by time variations of the equivalent depth, since H_e modulates the phase speed of the waves, given by $u_{\text{phase}} = \sqrt{\frac{f^2}{k^2} + (gH_e)^2}$ where k is the wavenumber. Space variations of H_e (along with the spatial variation of f) changes the wave propagation direction and its wavelength (Rainville & Pinkel, 2006).

Boundary conditions are designed to introduce and let out waves. They are of the radiative type (Blayo & Debreu, 2005). The amplitudes and directions of incoming waves are prescribed with a Flather condition (Flather, 1987) as:

$$v^n \pm \sqrt{\frac{g}{H_e}} \eta = v_{\text{ext}}^n \pm \sqrt{\frac{g}{H_e}} \eta_{\text{ext}} \quad (7)$$

where v^n is the normal component of the wave velocity at the boundary. Parameters v_{ext}^n and η_{ext} must be prescribed. The signs in the above equation vary with the boundary (− for southern and western boundaries, + for the others).

Incoming waves are superpositions of progressive monochromatic waves with frequency ω and absolute wavenumber k . The frequency is a tidal frequency (details are given in Section 5) and k is deduced from ω using the dispersion relation:

$$\omega^2 = gH_e k^2 + f^2 \quad (8)$$

The superposing, monochromatic waves differ by their amplitudes and their propagation directions. Denoting v_θ^n and η_θ the amplitudes of velocity and SSH of the wave entering the domain with an angle θ with the inward boundary normal direction, and denoting κ_θ the unit vector of the propagation direction, the expressions of parameters v_{ext}^n and η_{ext} at boundary grid point $\mathbf{r} = (x, y)$ and time t are:

$$\eta_{ext}[t, x, y] = \sum_{\theta} \Re \left(\underline{\eta_\theta}[t, x, y] e^{i(\omega t - k \kappa_\theta \cdot \mathbf{r})} \right), \quad (9a)$$

$$v_{ext}^n[t, x, y] = \sum_{\theta} \Re \left(\underline{v_\theta^n}[t, x, y] e^{i(\omega t - k \kappa_\theta \cdot \mathbf{r})} \right) \quad (9b)$$

where i is the imaginary unit and $\underline{\cdot}$ is the complex notation.

Parameters v_θ^n and η_θ are linked together by the polarisation relations (obtained from Equations 6). Thus, prescribing boundary conditions with Eq. 7 implies setting only η_θ at each boundary and for each angle θ . A limited number of angles are predefined. The prescription of the boundary conditions involves $2N_\theta N_b N_t$ values, with N_θ the number of prescribed wave directions, N_b the number of grid points at the boundary, and N_t the number of model time steps. In the following, we denote all these external values to be prescribed by η_{ext} .

3.2 4DVar cost function

The forward problem described in Section 3.1 is here formulated shortly as:

$$(u, v, \eta)_{t,x,y} = M(\phi) \quad (10)$$

where $\phi = (H_e, \eta_{ext})_{t,x,y}$ are the input parameters, M is the non linear operator solving the prognostic equations (6) associated with the OBCs (7) over a fixed time interval $[t_0, t_1]$. In Eq. 10, we neglect the initial condition in the function arguments. Given the high speed of the waves crossing the domain, we consider that the initial condition is quickly "forgotten" by the model, and the sea state simulated over a long enough time window essentially depends on boundary conditions.

The associated inverse problem consists in seeking the set of parameters $\phi^{\text{opt}} = (H_e^{\text{opt}}, \eta_{ext}^{\text{opt}})$ that produces a model state trajectory that best fits the observations η_{obs} in the time window $[t_0, t_1]$. We formulate this problem as the minimization of the 4DVar cost function:

$$J(\phi) = (\phi - \phi^b)^T B^{-1} (\phi - \phi^b) + (\eta_{\text{obs}} - H \cdot M(\phi))^T R^{-1} (\eta_{\text{obs}} - H \cdot M(\phi)) \quad (11)$$

where $\phi^b = (H_e^b, \eta_{ext}^b)$ is the background control vector, H is the linear operator that projects the model state in the observation space, B and R denote the background and observation error covariance matrices, respectively. In this work, these matrices are set diagonal.

The minimum of J is found using a descent method that requires the calculation of the gradient ∇J with respect to ϕ :

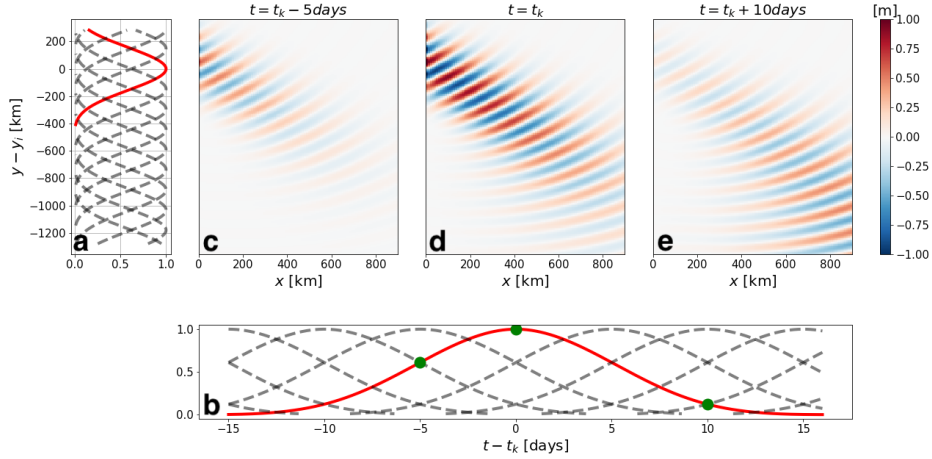


Figure 3. Illustration of the reduced-order basis for η_{ext} at the western border for $\theta = -\pi/4$: **(a)** the spatial decomposition with $\sigma = 150\text{km}$ (in red the spatial gaussian centered around y_i); **(b)** the temporal decomposition with $\tau = 5\text{days}$ (in red the temporal gaussian centered around t_k); **(c,d,e)** SSH snapshots produced by one element $G^{(k,i)}$ of the basis around the space-time coordinate (y_i, t_k) at three distinct times (represented by the green circles in **(b)**).

$$\nabla J(\phi) = 2B^{-1}(\phi - \phi^b) - 2M^* \cdot H^T \cdot R^{-1}(\eta_{\text{obs}} - H \cdot M(\phi)) \quad (12)$$

This gradient is computed with an adjoint method that makes use of the adjoint model M^* . Since the model M is non linear, an incremental 4Dvar algorithm (Courtier et al., 1994) is implemented to find the optimal set of parameters ϕ^{opt} that cancels ∇J .

3.3 Reduced-order 4Dvar

Order reduction is a standard practice in geophysical data assimilation or inversion, to overcome the issues of ill-posedness and numerical complexity (Blayo et al., 1998; Robert et al., 2005, e.g., for 4DVar). Control variables are projected into a low-dimensional basis of vectors (EOFs - Empirical Orthogonal Functions - are a usual choice, relevant to many inverse problems) and the cost function minimization is performed in this low-dimensional space to make it possible or faster.

In this work, we propose to express the control vector (i.e. the model parameters ϕ) in a reduced basis G made of space-time gaussian functions. This choice has been motivated by the fact that we know H_e and η_{ext} should vary "weakly" in space and time. Depth H_e inherits its time variation scales from the balanced flow, and the tidal forcing is quasi-stationary in comparison with the generated internal tides. Mathematically, we call $G^{(k,i)}$ one basis function centered at the point (t_k, r_i) (t_k is a timestamp and r_i is a spatial coordinate), expressed as:

$$G^{(k,i)}(t, r) = e^{-\left(\frac{(t-t_k)^2}{2\tau^2}\right)} e^{-\left(\frac{\|r-r_i\|^2}{2\sigma^2}\right)} \quad (13)$$

where τ (respectively σ) is the time (respectively space) characteristic scale. For H_e , r and r_i both refer to 2D coordinates (x, y) while for η_{ext} they refer to a 1D coordinate (along the

domain boundary). Thus, $G^{(k,i)}$ is a 3D function for H_e and a 2D function for η_{ext} . As an illustration, we represent in Figure 3 the space-time distribution of the basis functions for η_{ext} at the western boundary and the wavy SSH produced by one element of the basis. Two successive basis functions are separated by $t_{k+1} - t_k = \tau$ in time and $\|r_{i+1} - r_i\| = \sigma$ in space.

In this basis, ϕ writes as:

$$\phi = G \cdot w = \sum_k \sum_i w_{ki} G^{(k,i)} \quad (14)$$

where $w = (w_{ik})$ are the coordinates of ϕ in the basis G , and the new control variables of the 4DVar. The cost function J and its gradient ∇J are then obtained by replacing H by $H \cdot G$ in equations 11 and 12.

For the order reduction to be efficient, the characteristic scales τ and σ of the gaussian basis functions has to be carefully chosen. They should be short enough to explain a maximum of the variability of H_e and η_{ext} and long enough to reduce significantly the dimension of the control space. In the experiments presented in Section 5, the dimension of the control space is reduced by a factor of 10^4 .

In addition to reducing the size of the control vector, the reduced order basis justifies the choice of a diagonal matrix for B , assuming that the basis element are independent from each other.

4 Joint estimation approach

As stated literally in the introduction, our goal is to map and separate BM and IT based on SWOT observations that contains both components, and our approach is based on data assimilation. Let us represent by η^{BM} the SSH field related to BM, η^{IT} the SSH field related to IT, and η_{obs} the observation informing about $\eta^{BM} + \eta^{IT}$. The reconstruction problem is formulated as finding:

$$\arg \min_{\eta^{BM}, \eta^{IT}} \|\eta^{BM} + \eta^{IT} - \eta_{obs}\|^2 \quad (15)$$

where the norm typically considered here is the L_2 norm based on the space-time integral. The resolution of the minimization problem is addressed using a classical alternating minimization procedure (Tseng, 1990). The use of an alternating minimization algorithm is based on the strong assumption of the decoupling between the dynamics driving BM and IT. In reality, BM impact the propagation of IT. Here, the BM effect on IT propagation is introduced through the equivalent depth H_e only. Iterations are performed, alternating the two minimization subproblems:

$$\widehat{\eta_k^{BM}} = \arg \min_{\eta^{BM}} \|\eta^{BM} + \eta_{k-1}^{IT} - \eta_{obs}\|^2, \quad (16a)$$

$$\widehat{\eta_k^{IT}} = \arg \min_{\eta^{IT}} \|\widehat{\eta_k^{BM}} + \eta^{IT} - \eta_{obs}\|^2 \quad (16b)$$

In these equations, k is an iteration index. $\widehat{\eta_k^{BM}}$ and $\widehat{\eta_k^{IT}}$ are BM and IT estimations, respectively, at iteration k .

Both minimization subproblems in Eq. 16a and 16b can be solved with methods standard in geophysical data assimilation (4DVar, 3DVar, Kalman filters, etc). In what follows, Eq. 16a is solved with BFN-QG (see section 2) assimilating the corrected observation $\eta_{obs} - \eta_{k-1}^{IT}$.

Equation 16b is solved with 4DVar-SW (see section 3) assimilating the corrected observation $\eta_{\text{obs}} - \eta_k^{\text{BM}}$. The joint estimation pseudo-code is presented in Algorithm 1 and illustrated in Figure 1.

Algorithm 1: The joint estimation algorithm. Variables $\widehat{\eta}^{\text{BM}}$ and $\widehat{\eta}^{\text{IT}}$ are BM and IT estimations, respectively. K is a convergence criterion.

Result: $\widehat{\eta}^{\text{BM}}$ and $\widehat{\eta}^{\text{IT}}$
Initialize $\eta_{\text{obs}}^{\text{BM}} = \eta_{\text{obs}}$;
 $K = \text{True}$;
while K **do**
 1. Compute $\widehat{\eta}^{\text{BM}}$ from $\eta_{\text{obs}}^{\text{BM}}$ solving 16a ;
 2. Do $\eta_{\text{obs}}^{\text{IT}} = \eta_{\text{obs}} - \widehat{\eta}^{\text{BM}}$;
 3. Compute $\widehat{\eta}^{\text{IT}}$ from $\eta_{\text{obs}}^{\text{IT}}$ solving 16b ;
 4. Do $\eta_{\text{obs}}^{\text{BM}} = \eta_{\text{obs}} - \widehat{\eta}^{\text{IT}}$;
 5. Update K
end

5 Experiment setup

The joint estimation algorithm is tested with OSSEs (Observing System Simulation Experiments): a simulation provides reference surface data containing both BM and IT motions; SSH observations are extracted from this simulation and are assimilated; the estimated fields are then compared to the reference fields.

5.1 Reference simulation

The test flow consists of a turbulent zonal jet and a mode-1 internal tide propagating signal described in Ponte et al. (2017) and Dunphy et al. (2017). This simulation is carried out with the Coastal and Regional Ocean COmmunity (CROCO, <https://www.croco-ocean.org>) model. The horizontal resolution is 4 km and the domain size is 1024 km x 2880 km. The mode-one internal tide is generated by a zonally uniform tide excitation in the southern part of the domain. The time period of the tide is $T = 12$ hours. The plane wave produced is propagating northward and is encountering the meridional jet located at the center of the domain (Figure 2).

The reference SSH, called η_{truth} , is decomposed into BM and IT (Dunphy et al., 2017). The reference BM field $\eta_{\text{truth}}^{\text{BM}}$ is obtained by low pass filtering η_{truth} :

$$\eta_{\text{truth}}^{\text{BM}}(t) = \frac{1}{W} \int_{t-2T}^{t+2T} \eta_{\text{truth}}(t_i) e^{-\left(\frac{t_i-t}{T}\right)^2} dt_i$$

where $W = \int_{t-2T}^{t+2T} e^{-\left(\frac{t_i-t}{T}\right)^2} dt_i$. The reference IT field $\eta_{\text{truth}}^{\text{IT}}$, is obtained with an harmonic fitting:

$$\eta_{\text{truth}}^{\text{IT}}(t) = a_c(t) \cos\left(\frac{2\pi t}{T}\right) + a_s(t) \sin\left(\frac{2\pi t}{T}\right)$$

where:

$$a_c(t) = \frac{2}{W} \int_{t-2T}^{t+2T} \eta_{\text{truth}}(t_i) \cos\left(\frac{2\pi t_i}{T}\right) e^{-\left(\frac{t_i-t}{T}\right)^2} dt_i$$

$$a_s(t) = \frac{2}{W} \int_{t-2T}^{t+2T} \eta_{\text{truth}}(t_i) \sin\left(\frac{2\pi t_i}{T}\right) e^{-\left(\frac{t_i-t}{T}\right)^2} dt_i$$

Figure 2 shows snapshots of the total field, BM, and IT flows. The IT surface signature on SSH is not exceeding 5 cm, while BM's is around 50 cm. The IT wavelength is about 150 km. South of the jet, the wave is rectilinear and aligned with the southern boundary, which reflects its stationarity. North of the jet, the wave is dispersed due to its interaction with turbulent BM, producing nonstationarity in the wave field (Dunphy et al., 2017).

5.2 Observational scenari

Observations are drawn from the true SSH (η_{truth}), containing both BM and IT components. They are free of error, complete in space, and regularly distributed in time. The observation frequency is 75 h in the reference experiments discussed in Section 6.1.

In order to help evaluation of the mapping performance of the joint estimation experiments (hereafter denoted as *joint*), two additional scenari are considered. The first one, denoted *idealized*, refers to the case where both components can be observed separately, and each observation is processed with the appropriate assimilation system. This means that BFN-QG (4Dvar-SW) is fed with observations extracted from $\eta_{\text{truth}}^{\text{BM}}$ ($\eta_{\text{truth}}^{\text{IT}}$, respectively) fields. This ideal scenario provides upper bounds for the mapping performance of the *joint* experiments. The second scenario, hereafter denoted as *independent*, implements each assimilation system independently (without iteration) with observations of the full signal η_{obs} . This scenario provides a baseline to be outperformed by the *joint* experiments.

This study also investigates the impact of the observational temporal sampling on the mapping performances. For that purpose, a sensitivity experiment is performed and discussed in section 6.2.

5.3 Configuration of assimilation

Assimilation is performed in an inner domain of the reference simulation, illustrated by the black squares in Figure 2, to avoid the effects of boundary conditions and forcing in the reference simulation. The horizontal resolution is degraded to 16 km to reduce computational complexity, and the experiments are run over 4 months.

The BFN-QG (4Dvar-SW) parameters are listed in Table 1 (Table 2, respectively). For the *joint* scenario, the background values H_e^b and η_{ext}^b are updated at each iteration by the optimal values found at the previous iteration. We consider two values for the observation error covariance matrix R : 0.01 m for the *joint* and *idealized* scenari, 0.1 m for the *independent* scenario. The value for the *independent* scenario is higher to reflect representativeness errors and allow convergence of the 4Dvar-SW even with the presence of BM in the observations.

5.4 Diagnostics

For measuring the performance of the reconstruction, we use the time varying Root Mean Score Error (*RMSE*) and its associated score S , defined as follows:

Parameter	Description	Value
L_R	First Rossby radius of deformation	30 km
$K_0 dt$	(adimensionalised) Nudging coefficient	0.1
τ	Nudging time scale	2 days
T_{BFN}	BFN sliding time window length	15 days

Table 1. BFN-QG parameters

Parameter	Description	Value
θ	Entry angles of incoming waves	$-\pi/2, 0, \pi/2$
σ	Gaussian space scale	150 km
τ	Gaussian time scale	20 days
H_e^b	Background value for H_e	0.9 m
η_{ext}^b	Background value for η_{ext}	0 m
B_{H_e}	Background error for H_e	0.2 m
$B_{\eta_{ext}}$	Background error for η_{ext}	0.001 m
R	observational error	0.01 m or 0.1 m

Table 2. 4Dvar-SW parameters. As the covariance matrix (B and R) are diagonal, only standard deviations are given.

$$RMSE^{BM}(t) = \sqrt{\frac{1}{N} \sum_{i=1}^N \left(\widehat{\eta^{BM}}(t, i) - \eta_{truth}^{BM}(t, i) \right)^2}, \quad (17a)$$

$$S^{BM} = 1 - \frac{\overline{RMSE^{BM}}}{RMS\left(\eta_{truth}^{BM} - \overline{\eta_{truth}^{BM}}\right)}, \quad (17b)$$

$$RMSE^{IT}(t) = \sqrt{\frac{1}{N} \sum_{i=1}^N \left(\widehat{\eta^{IT}}(t, i) - \eta_{truth}^{IT}(t, i) \right)^2}, \quad (17c)$$

$$S^{IT} = 1 - \frac{\overline{RMSE^{IT}}}{RMS\left(\eta_{truth}^{IT}\right)} \quad (17d)$$

where N is the number of pixel in the study domain, \overline{X} is the time-average of the variable X and RMS is the root mean square function. A score of 1 indicates a perfect reconstruction in terms of $RMSE$, while a score of 0 indicates that the time-averaged $RMSE$ is as large as the RMS of the reference field. Note that for BM, the score is defined relative to the time anomaly of the reference field.

6 Results

6.1 Reconstruction performances

Figure 4 illustrates the performances of the joint estimation algorithm over the iterations for a temporal sampling of 75 h (6.25 IT periods). The joint estimation algorithm converges after 10 iterations. The scores obtained with the *idealized* and *independent* scenarii are also shown. As the joint estimation is started by a BM reconstruction, the first iteration of the joint algorithm corresponds to the *independent* scenario for BM.

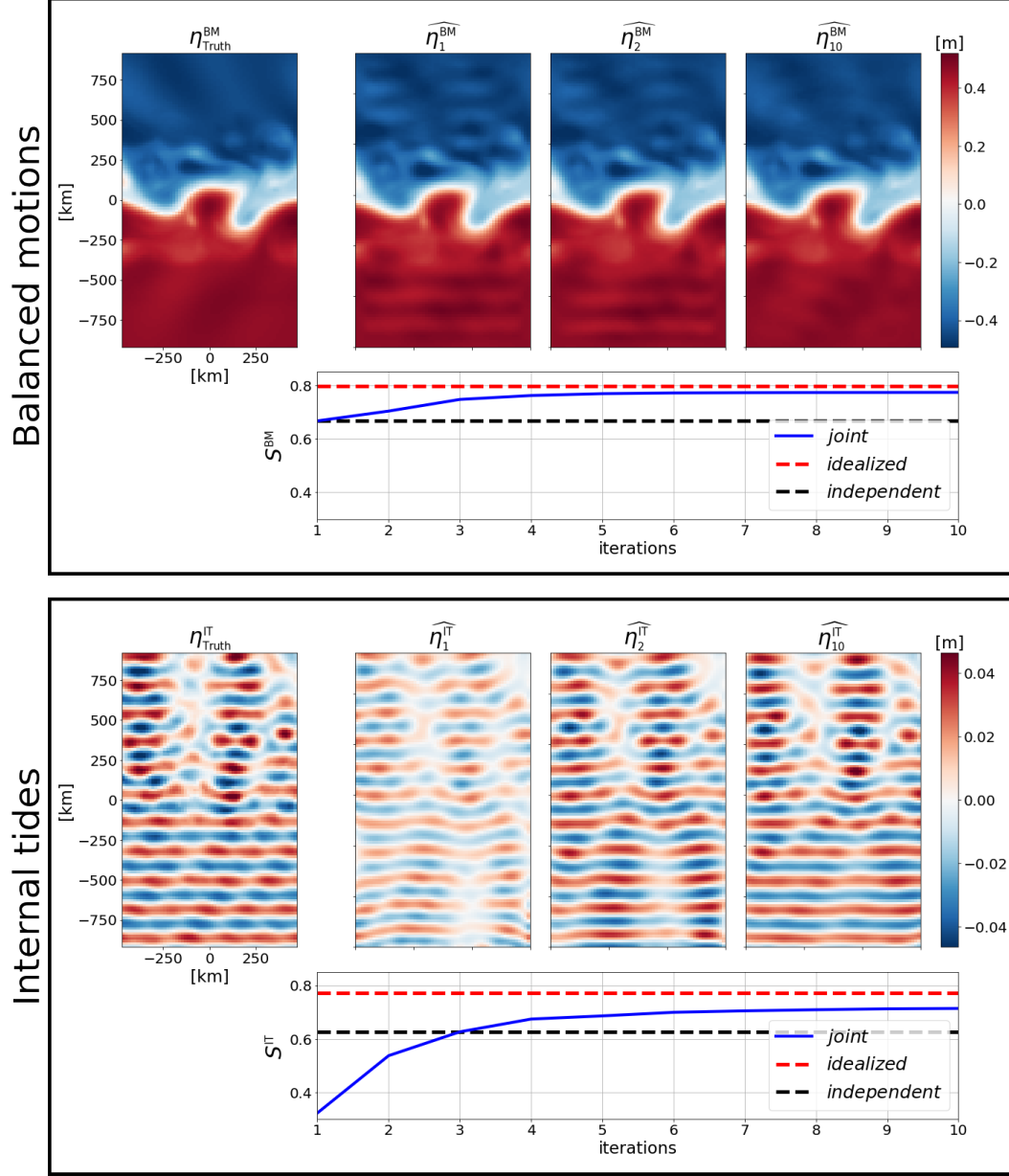


Figure 4. Performances of the estimation of BM (top) and IT (bottom). For each class of motion, snapshots at the first, the second, and the tenth iteration are shown. The evolution of the scores for the *joint* (solid blue curve), *idealized* (dash red curve) and *independent* (dash black curve) scenarii are plotted in function of the iterations of the joint estimation algorithm.

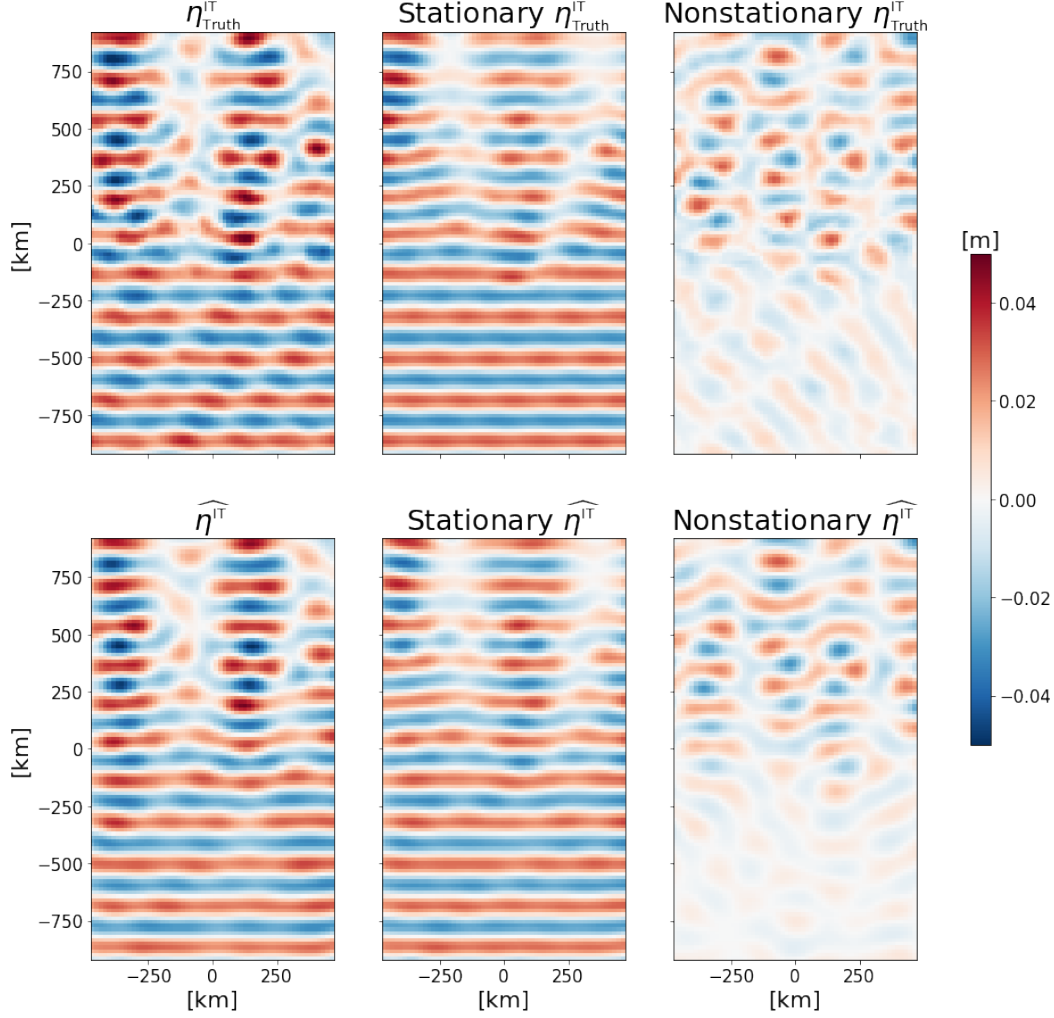


Figure 5. SSH snapshots of the IT field from the reference (top) and the reconstruction by the joint estimation algorithm (bottom). The full IT signal (left) is decomposed in the stationary (middle) and nonstationary (right) components.

Without the alternating minimization, the estimation scores for both BM and IT fall between 60% (worst case, *independent* scenario) and 80% (best case, *idealized* scenario). The 80% bound is likely due to the observation time sampling and to physical processes unresolved by the QG and SW models. These processes include the presence of higher baroclinic modes and ageostrophic dynamics for the QG model, higher tidal harmonics and neglected terms in the SW model. The lower 60% bound reflects the presence of the component that the system can not (or hardly) reconstruct (IT for the QG model, BM for the SW model). This component appears as noise in the observations.

The joint estimation algorithm is able to disentangle BM and IT components of SSH. Throughout iterations, both components are progressively separated. This is particularly visible in the $\widehat{\eta}^{\text{BM}}$ snapshots, where IT signature is clearly visible at the first iteration, and gradually filtered out throughout iterations. We attribute the strength of the joint estimation to the fact that each data assimilation sub-system (BFN-QG and 4DVar-SW) filters out the component it is not supposed to reconstruct. This is reflected in the relatively high (closer to 1 than 0) scores reached in the *independent* scenarios.

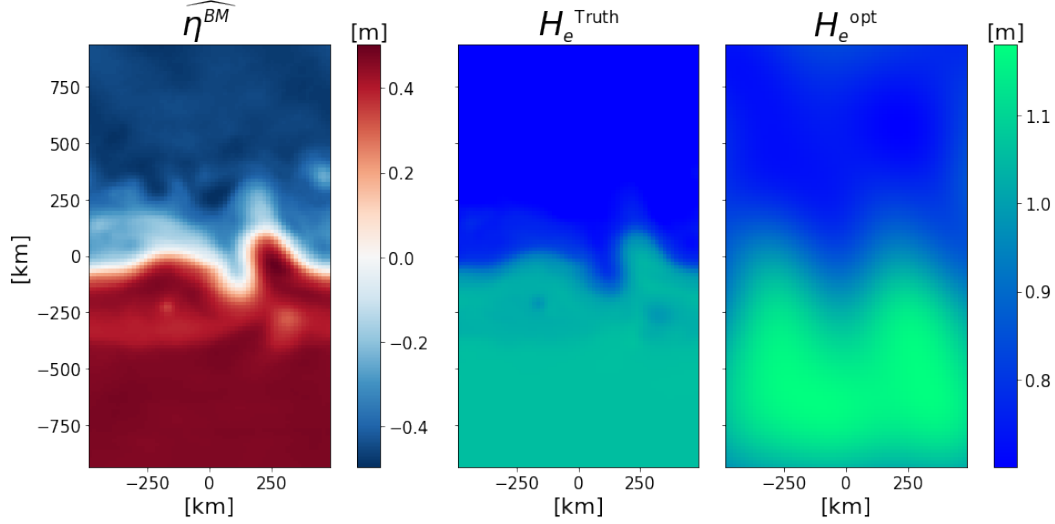


Figure 6. Left: BM SSH reconstructed by BFN-QG in the joint estimation algorithm. Middle: reference H_e computed from the 3D fields of the reference simulation. Right: H_e estimated by 4Dvar-SW in the joint estimation algorithm.

The 4Dvar-SW technique can reconstruct a large part of the nonstationary part of IT, as illustrated on Figure 5. 87 % of the stationary and 44% of the nonstationary IT variances are recovered on average. For the nonstationary IT fields, 4Dvar-SW captures 54% of the variance in the northern part of the domain, but only 28% in the southern part. This poor performance is attributed to the weakness of the nonstationary signal in the southern part (Figure 5, right column). Besides, some physical processes, such as IT reflection on the turbulent jet, may not be captured by 4Dvar-SW.

The spatial patterns of SSH $\widehat{\eta}^{BM}$ estimated by BFN-QG and the optimal equivalent depth H_e^{opt} obtained with 4Dvar-SW share similarities together and with the reference equivalent depth, as illustrated on Figure 6. A natural improvement of the method would be to use $\widehat{\eta}^{BM}$ to estimate a background value H_e^b in the 4Dvar-SW to improve the IT reconstruction. This would require a climatology of the stratification to convert SSH to H_e . Reciprocally, 4Dvar-SW could help refine the estimation of H_e and stratification.

6.2 Sensitivity to the observation temporal sampling

In this section we investigate the impact of the observation temporal sampling on the estimation of IT and BM. 13 time intervals Δt_{obs} are tested, from 69 h to 75 h by increments of 30 min. The IT period being $T=12$ h, the 6 h-interval length corresponds to $T/2$ and the central 72 h step corresponds to a multiple of T . For each Δt_{obs} , we run an *idealized*, an *independent* and an *joint* experiments. The results are shown on Figure 7.

The IT estimation is strongly degraded near $\Delta t_{\text{obs}}=72$ h, what affects the reconstruction of BM in the joint estimation. At $\Delta t_{\text{obs}}=72$ h, IT estimation scores are even negative in the *joint* and *independent* scenarios. This particular time interval presents a singularity and leads to an aliasing issue, since it observes only one phase of the wave field and does not detect the wave propagation. The same occurs with multiples of $T/2$ (e.g. 66 h and 78 h, not shown here), when only two opposite phases of the wave field are observed. Since the IT component is not filtered out by 4Dvar-SW, the estimation of BM by BFN-QG in the *joint* scenario is similar to the *independent* one.

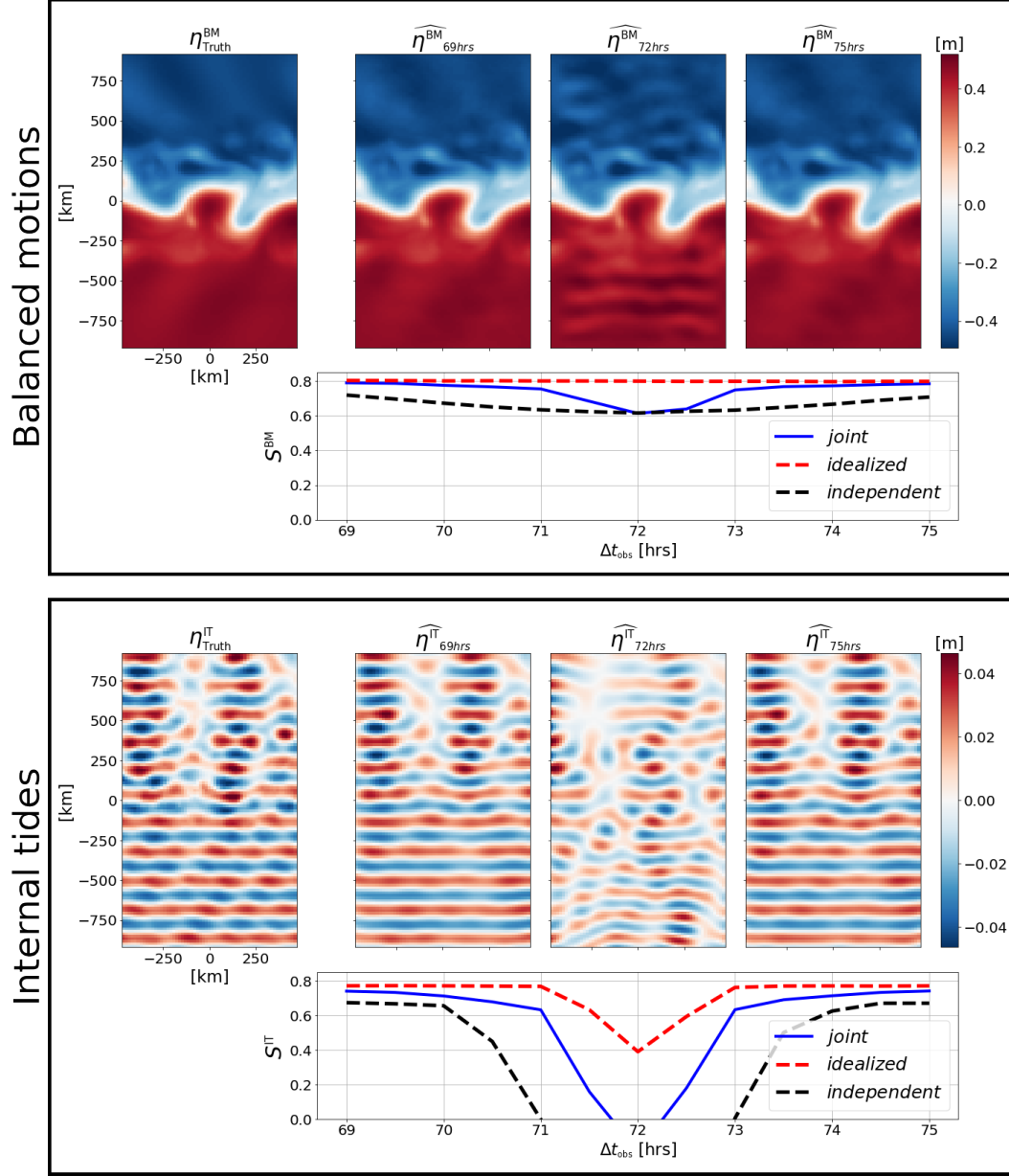


Figure 7. Performances of the joint estimation algorithm in function of the observation temporal sampling.

Using the joint estimation algorithm mitigates the poor IT reconstruction with time intervals near 72 h. The IT estimation scores with $\Delta t_{\text{obs}} = 71$ h or 73 h are negative in the *independent* experiments, but exceed 0.6 in the *joint* experiments. This suggested robustness of the joint estimation algorithm is encouraging for the processing of the future SWOT data.

7 Conclusions

In this study, we have presented an alternating minimization algorithm to simultaneously and dynamically map and separate Internal Tide (IT) and Balanced Motions (BM) signals from 2D altimetric observations. Two data assimilation techniques are used in an iterative process to estimate both signals: BM are reconstructed by the BFN-QG algorithm while IT are reconstructed by the 4Dvar-SW algorithm. At any given iteration, the assimilated observations used to map one signal are made of the difference between the full observation (containing both signals) and the previous estimation of the other signal. The use of the 4Dvar-SW algorithm for IT reconstruction allows to map (i.e., estimate in magnitude and phase) both stationary and nonstationary IT signals which is not obvious with other conventional separation methods such as harmonic analyses.

The joint estimation of BM and IT has been tested in an idealized context, with a true state of the ocean and artificial observations extracted from a numerical simulation that propagates a mode-one internal tide through a turbulent quasigeostrophic jet. This numerical experiment aims at illustrating the feasibility of this approach in a simplified context and should constitute a step closer to the processing of future SWOT data.

The results show that the joint estimation allows to simultaneously separate and estimate 78% and 75% of the BM and IT variance, respectively. The remaining variance is interpreted as being due to non resolved dynamics by the QG and SW models.

A sensitivity study of the observational temporal sampling has also been performed and shows that an unfortunate temporal sampling of the observations can be detrimental to the joint estimation performances. In particular, the performances of the IT reconstruction are considerably reduced when the time step between two consecutive observations is a multiple of half the IT time period $T/2$. Fortunately, it turns out that this situation is singular for non sun-synchronous orbits, meaning that a slight shift from a multiple of $T/2$ in the observation time sampling ensures good performances again.

Although the results of the observational temporal sampling sensitivity study are encouraging, future work should investigate the method applied to a realistic SWOT sampling. One of the major next steps will be to assess the potential of the method with spatially sparse observations. An interesting avenue to improve the method in that context could be to use additional information, such as conventional nadir data or SWOT nadir data, to ensure the joint estimation method convergence hence improving the reconstructions.

Another crucial step towards operational SSH mapping will be to experiment on a more realistic ocean simulation, with multiple tidal components and harmonics in constant interaction. To allow the 4Dvar-SW to efficiently extract IT signal from realistic SSH data, some technical improvement may be needed. Source terms, that generate IT signal inside the study domain, may have to be implemented and controlled by the assimilation to map IT signals around generation sites (located at ocean ridge and sea mounts for instance). One can also think of improving the resolved dynamics by including higher baroclinic modes. Another improvement would be to add interaction terms between BM and IT in the shallow water equations. For that last remark, one strategy would be to estimate a background term of H_e from the reconstruction of BM.

Acknowledgments

This research was funded by ANR (project number ANR-17-CE01-0009-01) and CNES through the SWOT Science Team program. The numerical codes and the data used in this study can be accessed here: <https://github.com/leguillf/MASSH>

References

- Ajayi, A., Le Sommer, J., Chassignet, E., Molines, J.-M., Xu, X., Albert, A., & Dewar, W. (2019). Diagnosing cross-scale kinetic energy exchanges from two submesoscale permitting ocean models. *Earth and Space Science Open Archive*, 26. Retrieved from <https://www.essoar.org/doi/abs/10.1002/essoar.10501077.1> doi: 10.1002/essoar.10501077.1
- Ajayi, A., Sommer, J. L., Chassignet, E., Molines, J.-M., Xu, X., Albert, A., & Cosme, E. (2020). Spatial and temporal variability of the north atlantic eddy field from two kilometric-resolution ocean models. *Journal of Geophysical Research: Oceans*, 125(5), e2019JC015827. Retrieved 2020-06-15, from <https://agupubs.onlinelibrary.wiley.com/doi/abs/10.1029/2019JC015827> (_eprint: <https://agupubs.onlinelibrary.wiley.com/doi/pdf/10.1029/2019JC015827>) doi: 10.1029/2019JC015827
- Amores, A., Jord  , G., Arsouze, T., & Le Sommer, J. (2018). Up to what extent can we characterize ocean eddies using present-day gridded altimetric products? *Journal of Geophysical Research: Oceans*, 123(10), 7220-7236. Retrieved from <https://agupubs.onlinelibrary.wiley.com/doi/abs/10.1029/2018JC014140> doi: <https://doi.org/10.1029/2018JC014140>
- Anthes, R. (1974). Data assimilation and initialization of hurricane prediction models. *J. Atmos. Sci.*, 31, 701-719.
- Auroux, D., & Blum, J. (2008). A nudging-based data assimilation method: the back and forth nudging (BFN) algorithm. *Nonlinear Process Geophys.*, 15(2), 305-319. (Place: Gottingen Publisher: Copernicus Gesellschaft MbH WOS:000255511000007) doi: 10.5194/npg-15-305-2008
- Ballarotta, M., Ubelmann, C., Pujol, M.-I., Taburet, G., Fournier, F., Legeais, J.-F., . . . Picot, N. (2019). On the resolutions of ocean altimetry maps. *Ocean Sci.*, 15(4), 1091-1109. (Place: Gottingen Publisher: Copernicus Gesellschaft MbH WOS:000481992900001) doi: 10.5194/os-15-1091-2019
- Blayo, E., Blum, J., & Verron, J. (1998). Assimilation variationnelle de donn  es en oc  anographie et r  duction de la dimension de lâ  espace de contr  le (variational data assimilation in oceanography and reduction of the control-space dimension).
- Blayo, E., & Debreu, L. (2005). Revisiting open boundary conditions from the point of view of characteristic variables. *Ocean Modelling*. Retrieved from <https://hal.inria.fr/inria-00134856>
- Capet, X., Roulet, G., Klein, P., & Maze, G. (2016, 11). Intensification of Upper-Ocean Submesoscale Turbulence through Charney Baroclinic Instability. *Journal of Physical Oceanography*, 46(11), 3365-3384. Retrieved from <https://doi.org/10.1175/JPO-D-16-0050.1> doi: 10.1175/JPO-D-16-0050.1
- Courtier, P., Th  paut, J., & Hollingsworth, A. (1994). A strategy for operational implementation of 4d  Rvar, using an incremental approach. *Quarterly Journal of the Royal Meteorological Society*, 120, 1367-1387.
- DIMET, F.-X. L., & TALAGRAND, O. (1986). Variational algorithms for analysis and assimilation of meteorological observations: theoretical aspects. *Tellus A*, 38A(2), 97-110. Retrieved from <https://onlinelibrary.wiley.com/doi/abs/10.1111/j.1600-0870.1986.tb00459.x> doi: <https://doi.org/10.1111/j.1600-0870.1986.tb00459.x>
- Dunphy, M., Ponte, A., Klein, P., & Gentil, S. (2017, 01). Low-mode internal tide propagation in a turbulent eddy field. *Journal of Physical Oceanography*, 47. doi: 10.1175/JPO-D-16-0099.1

- Flather, R. (1987). A tidal model of the northeast pacific. *Atmosphere-Ocean*, 25(1), 22–45. Retrieved from <https://doi.org/10.1080/07055900.1987.9649262> (Publisher: Taylor & Francis) doi: 10.1080/07055900.1987.9649262
- Fu, L.-L., & Ubelmann, C. (2014). On the transition from profile altimeter to swath altimeter for observing global ocean surface topography. *Journal of Atmospheric and Oceanic Technology*, 31(2), 560 - 568. Retrieved from https://journals.ametsoc.org/view/journals/atot/31/2/jtech-d-13-00109_1.xml doi: 10.1175/JTECH-D-13-00109.1
- Garrett, C., & Kunze, E. (2007). Internal tide generation in the deep ocean. *Annual Review of Fluid Mechanics*, 39(1), 57-87. Retrieved from <https://doi.org/10.1146/annurev.fluid.39.050905.110227> doi: 10.1146/annurev.fluid.39.050905.110227
- Gill, A. E. (1982). Atmosphere-ocean dynamics. *Int. Geophys. Ser.*, 30, 662p.
- Gonzalez-Haro, C., Isern-Fontanet, J., Tandeo, P., & Autret, E. (2019, May). High-resolution currents from the synergy between Infrared SST and altimetry. *LPS 2019 : Living Planet Symposium*.
- Guillou, F. L., Metref, S., Cosme, E., Ubelmann, C., Ballarotta, M., Sommer, J. L., & Verron, J. (2021). Mapping altimetry in the forthcoming swot era by back-and-forth nudging a one-layer quasigeostrophic model. *Journal of Atmospheric and Oceanic Technology*, 38(4), 697 - 710. Retrieved from <https://journals.ametsoc.org/view/journals/atot/38/4/JTECH-D-20-0104.1.xml> doi: 10.1175/JTECH-D-20-0104.1
- Haren, H. v., Laurent, L. S., & Marshall, D. (2004). Small and mesoscale processes and their impact on the large scale: an introduction. , 51(25), 2883–2887. Retrieved from <https://www.sciencedirect.com/science/article/pii/S0967064504002061> doi: <https://doi.org/10.1016/j.dsr2.2004.09.010>
- Kelly, S. M., & Lermusiaux, P. F. J. (2016). Internal-tide interactions with the gulf stream and middle atlantic bight shelfbreak front. *Journal of Geophysical Research: Oceans*, 121(8), 6271-6294. Retrieved from <https://agupubs.onlinelibrary.wiley.com/doi/abs/10.1002/2016JC011639> doi: <https://doi.org/10.1002/2016JC011639>
- Klein, P., & Lapeyre, G. (2009, 01). The oceanic vertical pump induced by mesoscale and submesoscale turbulence. *Annual review of marine science*, 1, 351-75. doi: 10.1146/annurev.marine.010908.163704
- McWilliams, J. C. (2016). Submesoscale currents in the ocean. *Proceedings of the Royal Society A: Mathematical, Physical and Engineering Sciences*, 472(2189), 20160117. Retrieved from <https://royalsocietypublishing.org/doi/abs/10.1098/rspa.2016.0117> doi: 10.1098/rspa.2016.0117
- Morrow, R., Fu, L.-L., Arduin, F., Benkiran, M., Chapron, B., Cosme, E., . . . Zaron, E. D. (2019). Global observations of fine-scale ocean surface topography with the surface water and ocean topography (swot) mission. *Frontiers in Marine Science*, 6, 232. Retrieved from <https://www.frontiersin.org/article/10.3389/fmars.2019.00232> doi: 10.3389/fmars.2019.00232
- Nash, J., Kelly, S., Shroyer, E., Moum, J., & Duda, T. (2012, 11). The unpredictable nature of internal tides on continental shelves. *Journal of Physical Oceanography*, 42, 1981-2000. doi: 10.1175/JPO-D-12-028.1
- Nelson, A. D., Arbic, B. K., Zaron, E. D., Savage, A. C., Richman, J. G., Buijsman, M. C., & Shriver, J. F. (2019). Toward realistic nonstationarity of semidiurnal baroclinic tides in a hydrodynamic model. *Journal of Geophysical Research: Oceans*, 124(9), 6632-6642. Retrieved from <https://agupubs.onlinelibrary.wiley.com/doi/abs/10.1029/2018JC014737> doi: <https://doi.org/10.1029/2018JC014737>
- Ponte, A. L., & Klein, P. (2015, March). Incoherent signature of internal tides on sea level in idealized numerical simulations. *Geophysical Research Letters*, 42(5), 1520-1526. Retrieved from <https://hal.archives-ouvertes.fr/hal-01149664> doi: 10.1002/2014GL062583

- 538 Ponte, A. L., Klein, P., Dunphy, M., & Le Gentil, S. (2017). Low-mode internal tides and
539 balanced dynamics disentanglement in altimetric observations: Synergy with surface
540 density observations. *Journal of Geophysical Research: Oceans*, 122(3), 2143-
541 2155. Retrieved from [https://agupubs.onlinelibrary.wiley.com/doi/abs/](https://agupubs.onlinelibrary.wiley.com/doi/abs/10.1002/2016JC012214)
542 [10.1002/2016JC012214](https://agupubs.onlinelibrary.wiley.com/doi/abs/10.1002/2016JC012214) doi: 10.1002/2016JC012214
- 543 Qiu, B., Chen, S., Klein, P., Wang, J., Torres, H., Fu, L.-L., & Menemenlis, D. (2018, 01).
544 Seasonality in transition scale from balanced to unbalanced motions in the world
545 ocean. *Journal of Physical Oceanography*, 48. doi: 10.1175/JPO-D-17-0169.1
- 546 Rainville, L., & Pinkel, R. (2006). Propagation of low-mode internal waves through the
547 ocean. , 36(6), 1220 – 1236. Retrieved from [https://journals.ametsoc.org/](https://journals.ametsoc.org/view/journals/phoc/36/6/jpo2889.1.xml)
548 [view/journals/phoc/36/6/jpo2889.1.xml](https://journals/phoc/36/6/jpo2889.1.xml) (Place: Boston MA, USA Publisher:
549 American Meteorological Society) doi: 10.1175/JPO2889.1
- 550 Ray, R. D., & Zaron, E. D. (2011). Non-stationary internal tides observed with satellite al-
551 timetry. *Geophysical Research Letters*, 38(17). Retrieved from [https://agupubs](https://agupubs.onlinelibrary.wiley.com/doi/abs/10.1029/2011GL048617)
552 [.onlinelibrary.wiley.com/doi/abs/10.1029/2011GL048617](https://agupubs.onlinelibrary.wiley.com/doi/abs/10.1029/2011GL048617) doi: [https://doi](https://doi.org/10.1029/2011GL048617)
553 [.org/10.1029/2011GL048617](https://doi.org/10.1029/2011GL048617)
- 554 Ray, R. D., & Zaron, E. D. (2015, 12). M2 Internal Tides and Their Observed Wavenum-
555 ber Spectra from Satellite Altimetry*. *Journal of Physical Oceanography*, 46(1), 3-22.
556 Retrieved from <https://doi.org/10.1175/JPO-D-15-0065.1> doi: 10.1175/JPO
557 -D-15-0065.1
- 558 Ray, R. D., & Zaron, E. D. (2016). M2 internal tides and their observed wavenumber spectra
559 from satellite altimetry. , 46(1), 3 – 22. Retrieved from [https://journals.ametsoc](https://journals.ametsoc.org/view/journals/phoc/46/1/jpo-d-15-0065.1.xml)
560 [.org/view/journals/phoc/46/1/jpo-d-15-0065.1.xml](https://journals/phoc/46/1/jpo-d-15-0065.1.xml) (Place: Boston MA,
561 USA Publisher: American Meteorological Society) doi: 10.1175/JPO-D-15-0065.1
- 562 Robert, C., Durbiano, S., Blayo, E., Verron, J., Blum, J., & Le Dimet, F.-X. (2005, Aug). A
563 reduced-order strategy for 4d-var data assimilation. *Journal of Marine Systems*, 57(1-
564 2), 70–82. Retrieved from [http://dx.doi.org/10.1016/j.jmarsys.2005.04](http://dx.doi.org/10.1016/j.jmarsys.2005.04.003)
565 [.003](http://dx.doi.org/10.1016/j.jmarsys.2005.04.003) doi: 10.1016/j.jmarsys.2005.04.003
- 566 Sadourny, R. (1975). The dynamics of finite-difference models of the shallow-water equa-
567 tions. , 32(4), 680 – 689. Retrieved from [https://journals.ametsoc.org/view/](https://journals.ametsoc.org/view/journals/atsc/32/4/1520-0469_1975_032_0680_tdoftdm_2_0_co_2.xml)
568 journals/atsc/32/4/1520-0469_1975_032_0680_tdoftdm_2_0_co_2.xml
569 (Place: Boston MA, USA Publisher: American Meteorological Society) doi:
570 10.1175/1520-0469(1975)032<0680:TDOFDM>2.0.CO;2
- 571 Taburet, G., Sanchez-Roman, A., Ballarotta, M., Pujol, M.-I., Legeais, J.-F., Fournier,
572 F., ... Dibarboue, G. (2019). DUACS DT2018: 25 years of reprocessed sea
573 level altimetry products. *Ocean Science*, 15(5), 1207–1224. Retrieved from
574 <https://www.ocean-sci.net/15/1207/2019/> (Publisher: Copernicus GmbH)
575 doi: <https://doi.org/10.5194/os-15-1207-2019>
- 576 Torres, H. S., Klein, P., Siegelman, L., Qiu, B., Chen, S., Ubelmann, C., ... Fu, L.-
577 L. (2019). Diagnosing ocean-wave-turbulence interactions from space. *Geo-*
578 *physical Research Letters*, 46(15), 8933-8942. Retrieved from [https://](https://agupubs.onlinelibrary.wiley.com/doi/abs/10.1029/2019GL083675)
579 agupubs.onlinelibrary.wiley.com/doi/abs/10.1029/2019GL083675 doi:
580 10.1029/2019GL083675
- 581 Tseng, P. (1990). Further applications of a splitting algorithm to decomposition in variational
582 inequalities and convex programming. , 48(1), 249–263. Retrieved from [https://doi](https://doi.org/10.1007/BF01582258)
583 [.org/10.1007/BF01582258](https://doi.org/10.1007/BF01582258) doi: 10.1007/BF01582258
- 584 Ubelmann, C., Klein, P., & Fu, L.-L. (2015). Dynamic interpolation of sea surface height
585 and potential applications for future high-resolution altimetry mapping. *J. Atmos.*
586 *Ocean. Technol.*, 32(1), 177–184. (Place: Boston Publisher: Amer Meteorological Soc
587 WOS:000348221100011) doi: 10.1175/JTECH-D-14-00152.1
- 588 Wunsch, C., & Ferrari, R. (2004). VERTICAL MIXING, ENERGY, AND THE GEN-
589 ERAL CIRCULATION OF THE OCEANS. , 36(1), 281–314. Retrieved 2021-03-29,
590 from [http://arjournals.annualreviews.org/doi/abs/10.1146%2Fannurev](http://arjournals.annualreviews.org/doi/abs/10.1146%2Fannurev.fluid.36.050802.122121)
591 [.fluid.36.050802.122121](http://arjournals.annualreviews.org/doi/abs/10.1146%2Fannurev.fluid.36.050802.122121) doi: 10.1146/annurev.fluid.36.050802.122121
- 592 Zaron, E. D. (2017). Mapping the nonstationary internal tide with satellite altimetry. *Jour-*

593 *nal of Geophysical Research: Oceans*, 122(1), 539-554. Retrieved from [https://](https://agupubs.onlinelibrary.wiley.com/doi/abs/10.1002/2016JC012487)
594 agupubs.onlinelibrary.wiley.com/doi/abs/10.1002/2016JC012487 doi:
595 10.1002/2016JC012487

Figure 1.

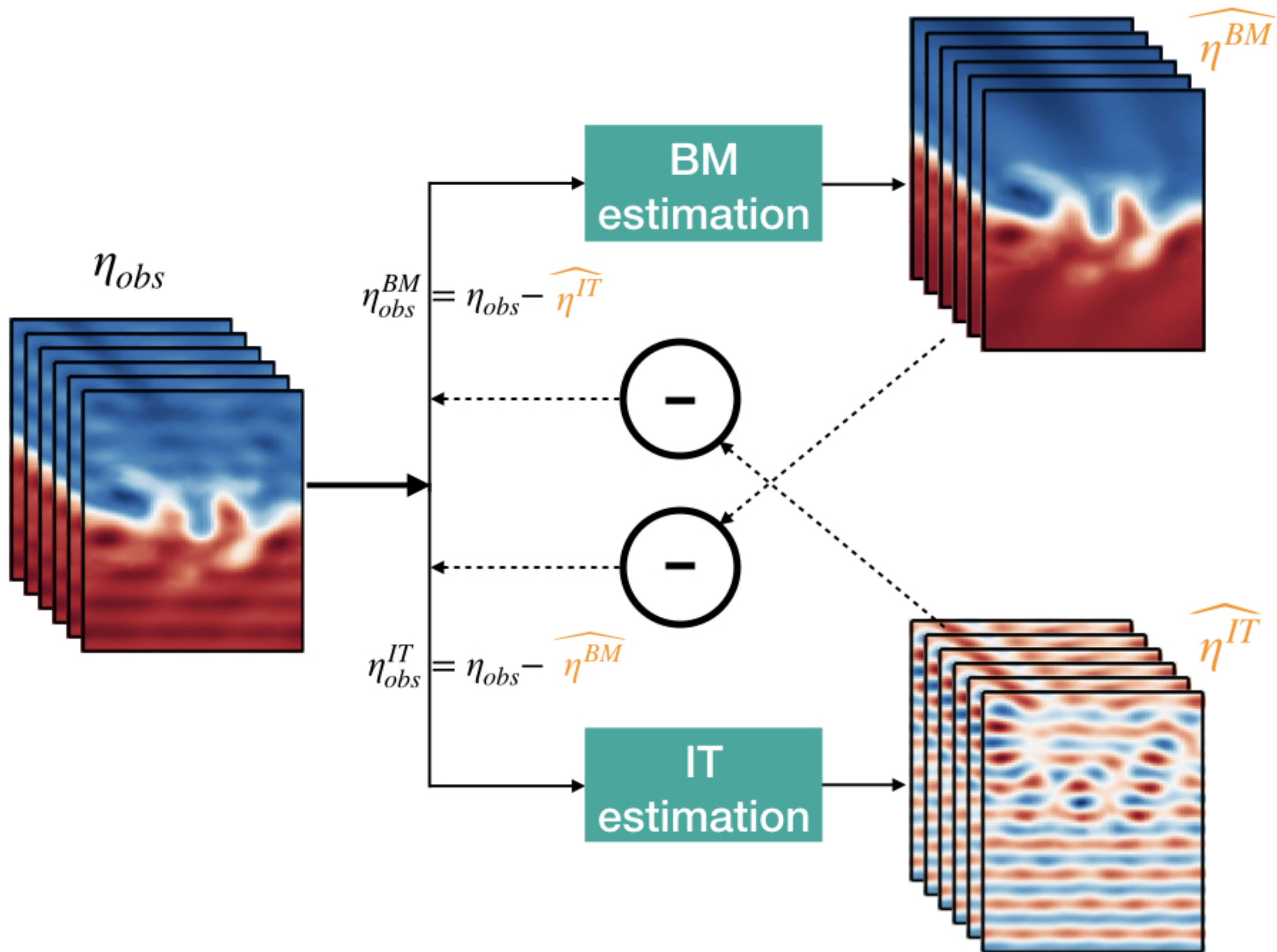


Figure 2.

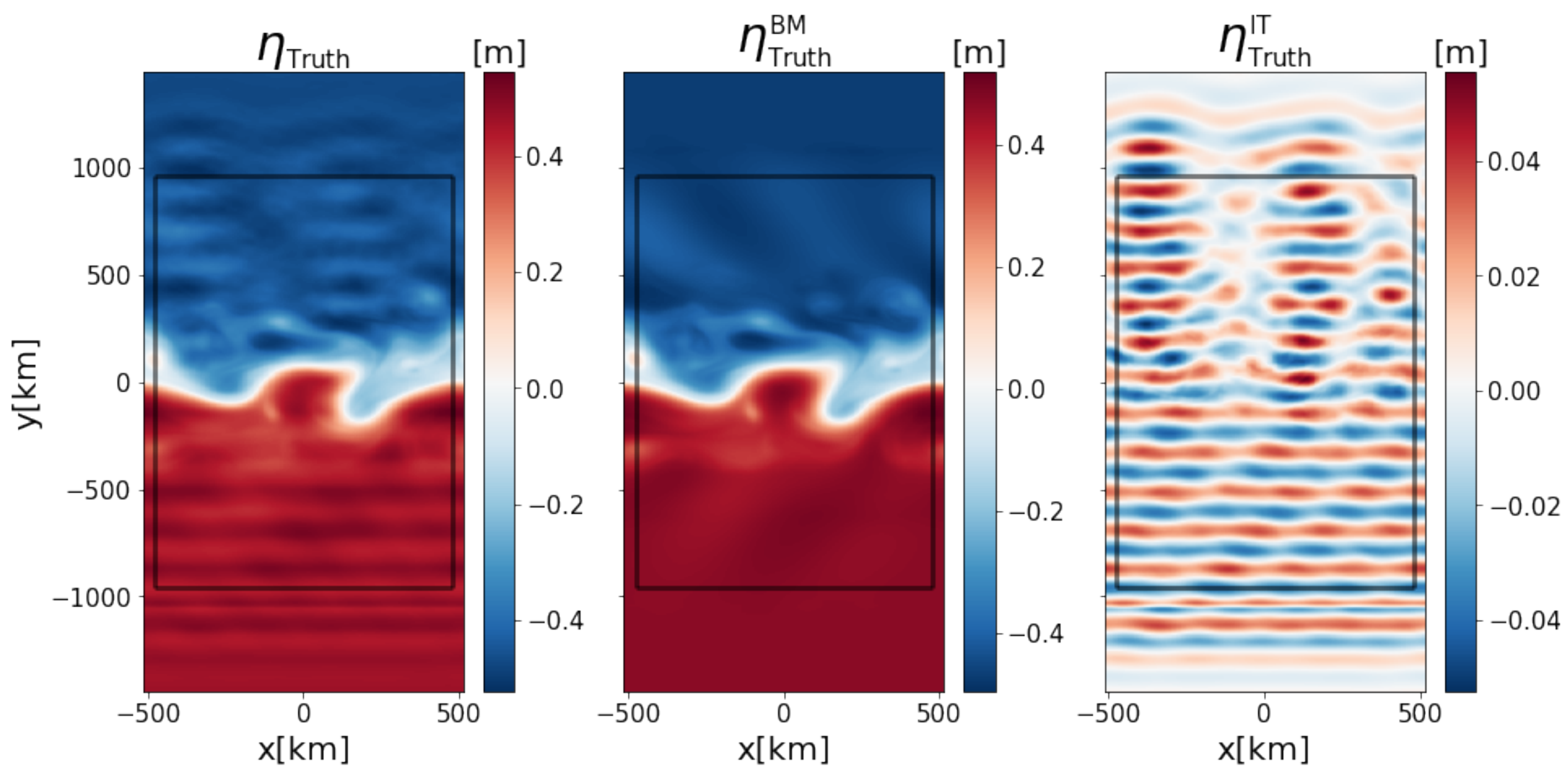


Figure 3.

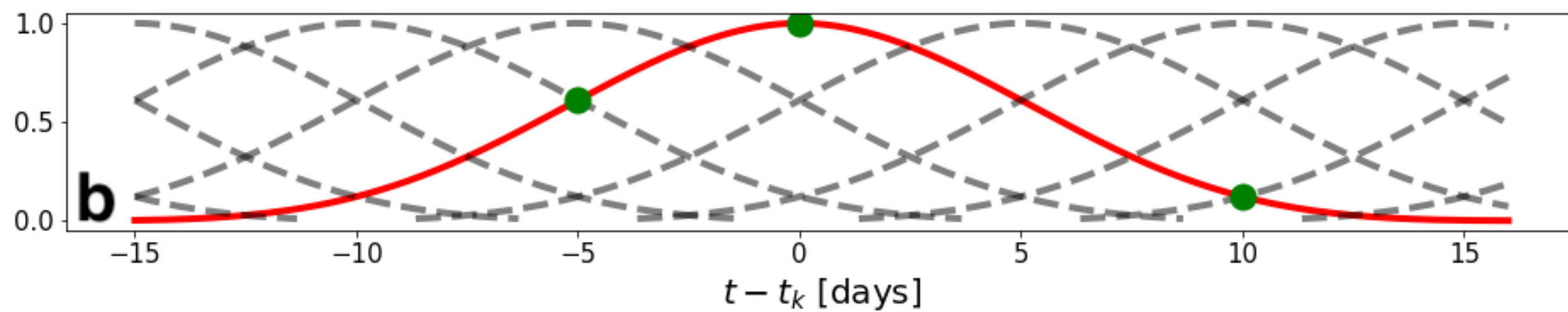
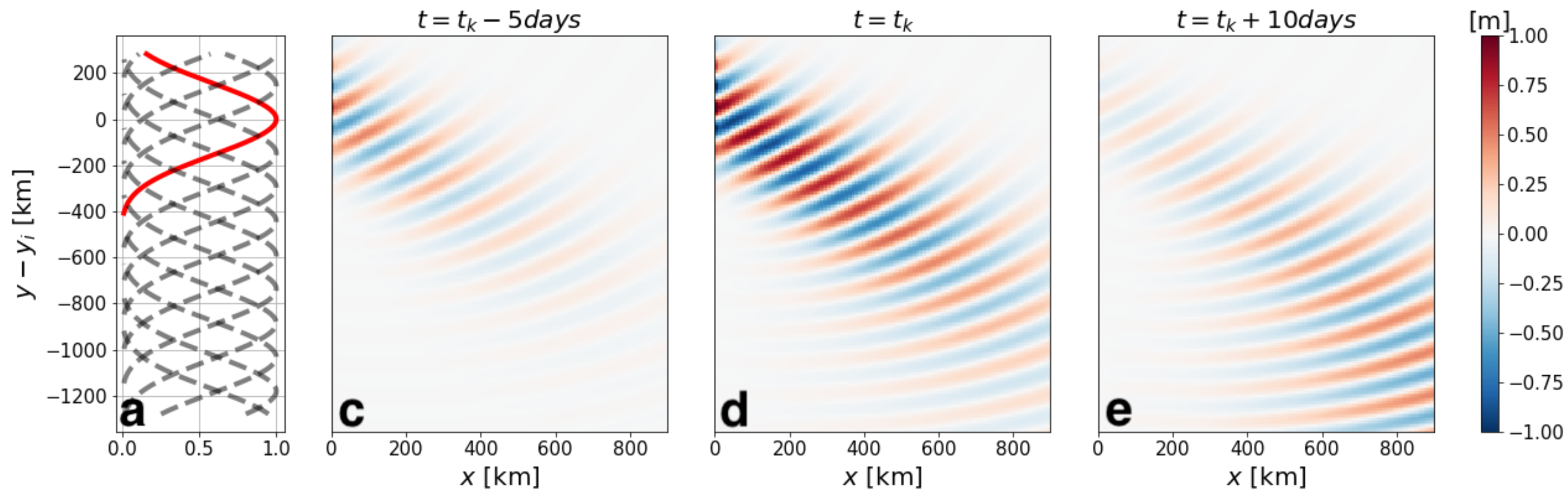
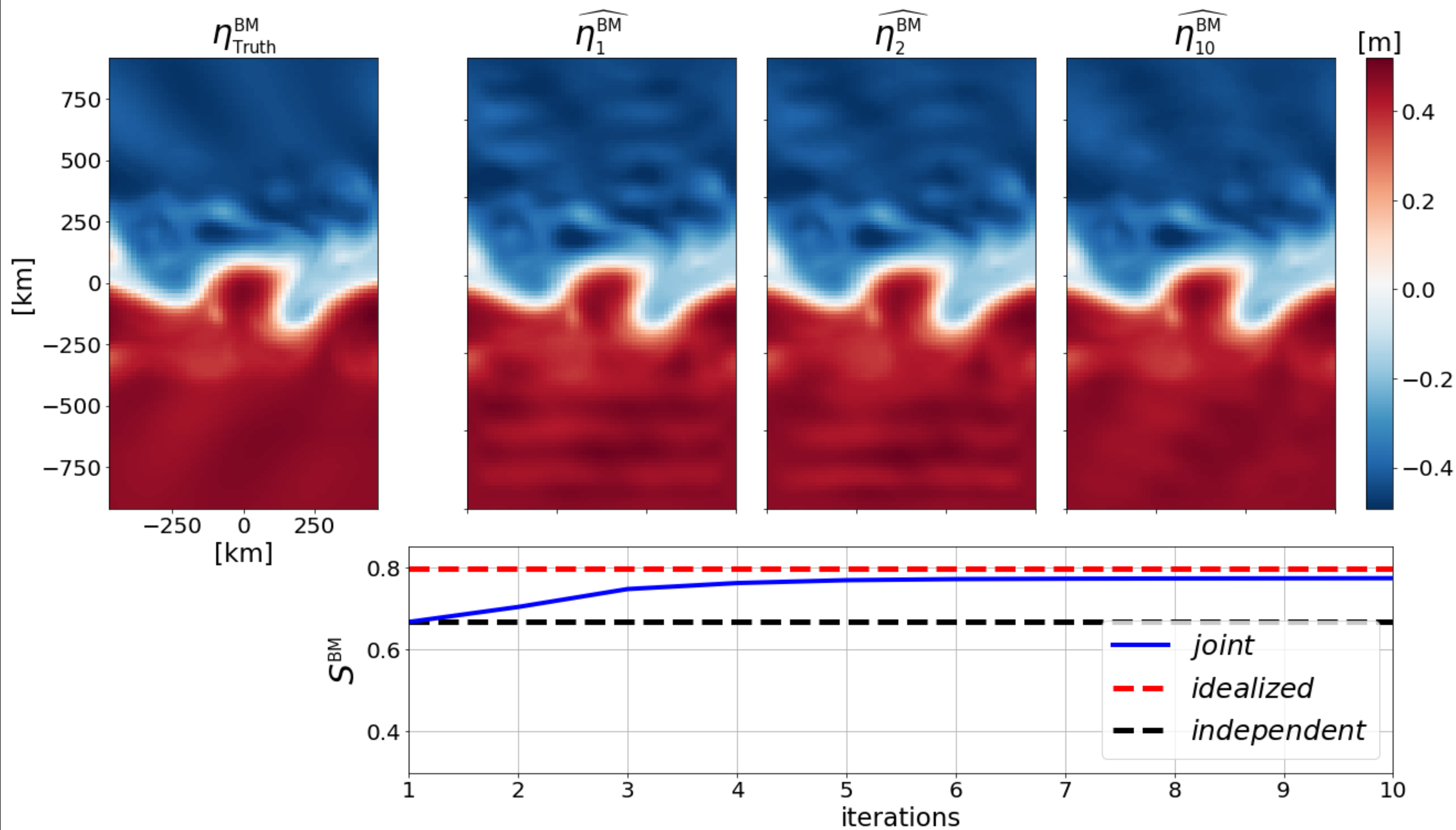


Figure 4.

Balanced motions



Internal tides

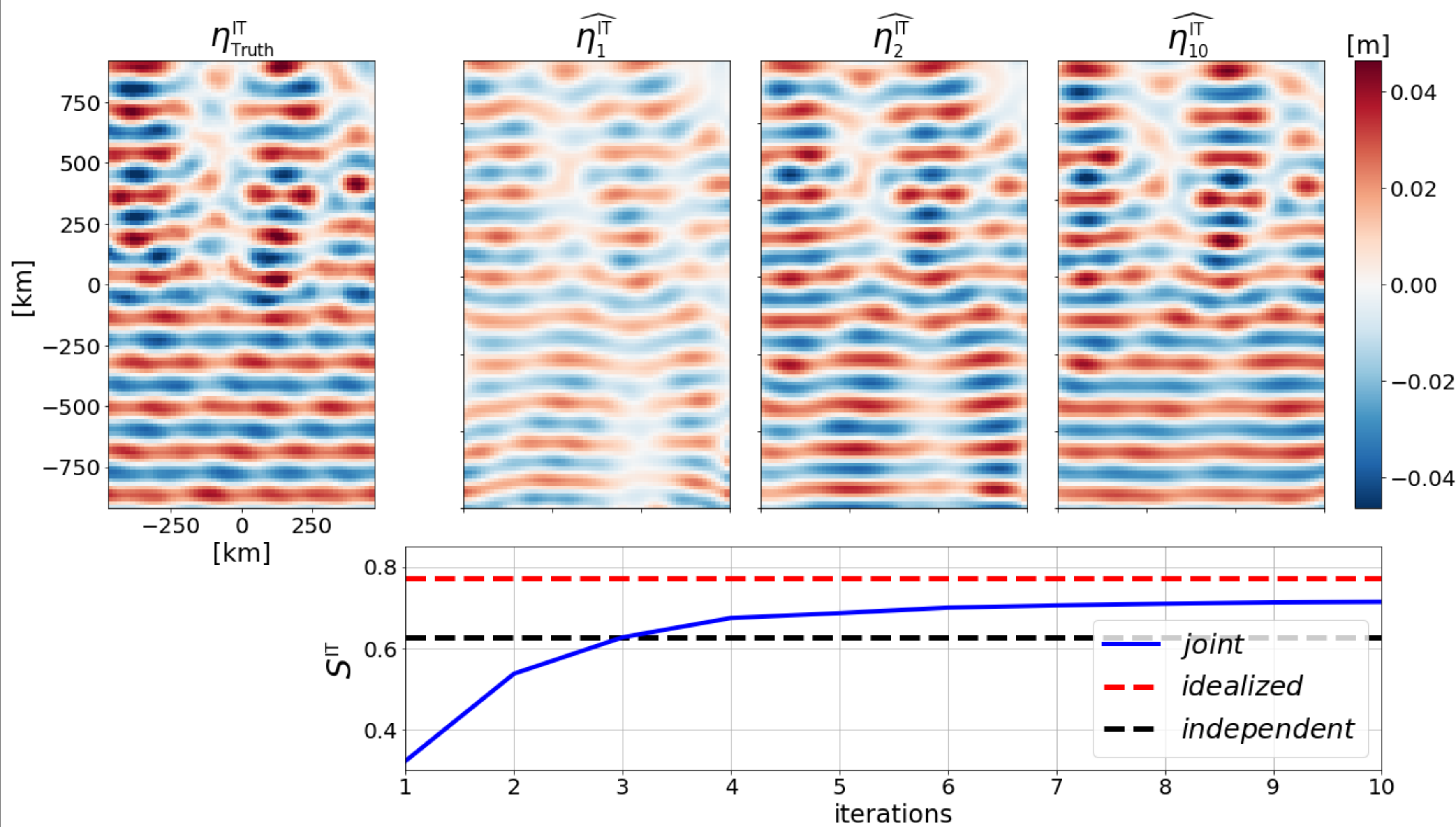


Figure 5.

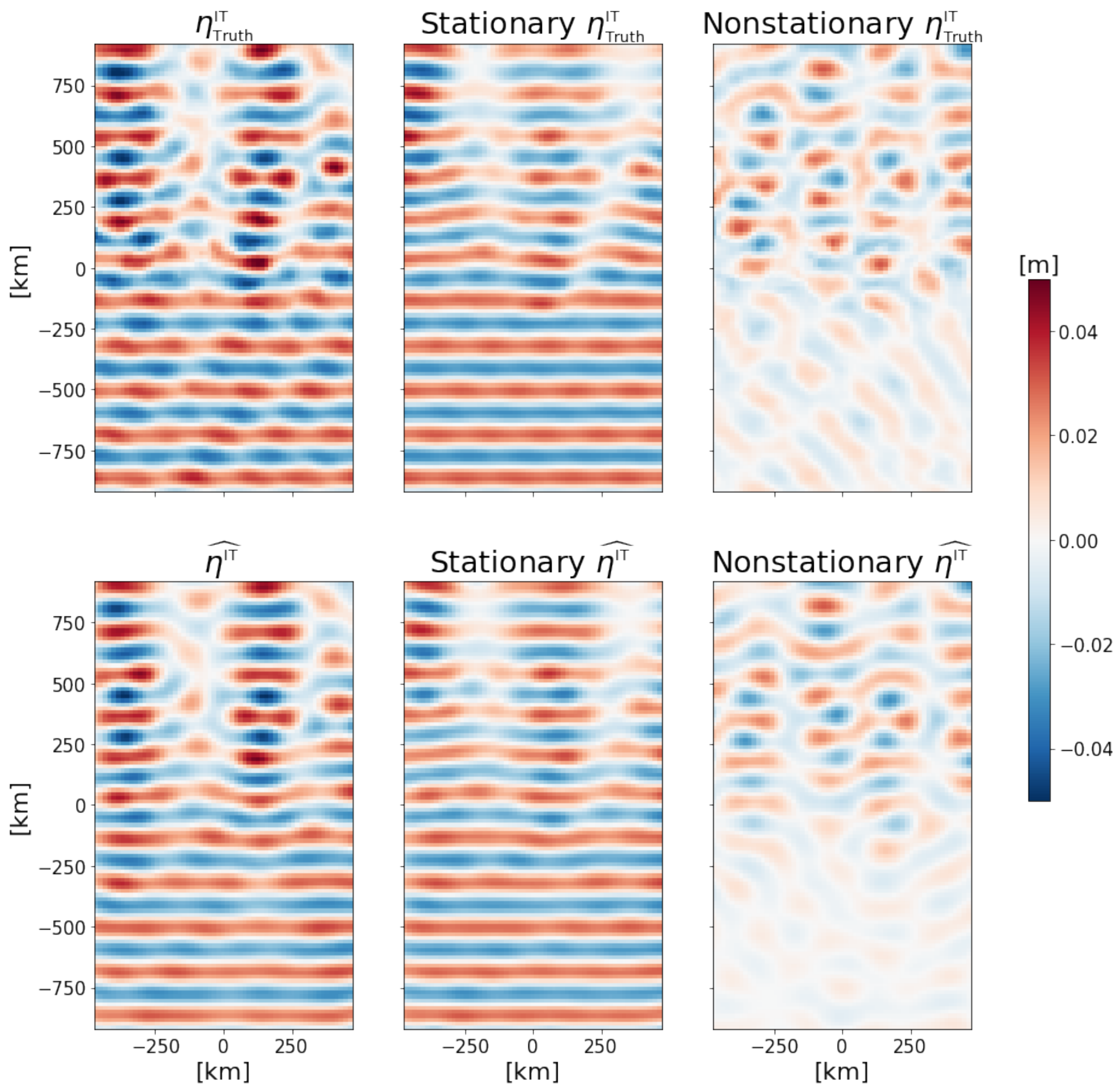


Figure 6.

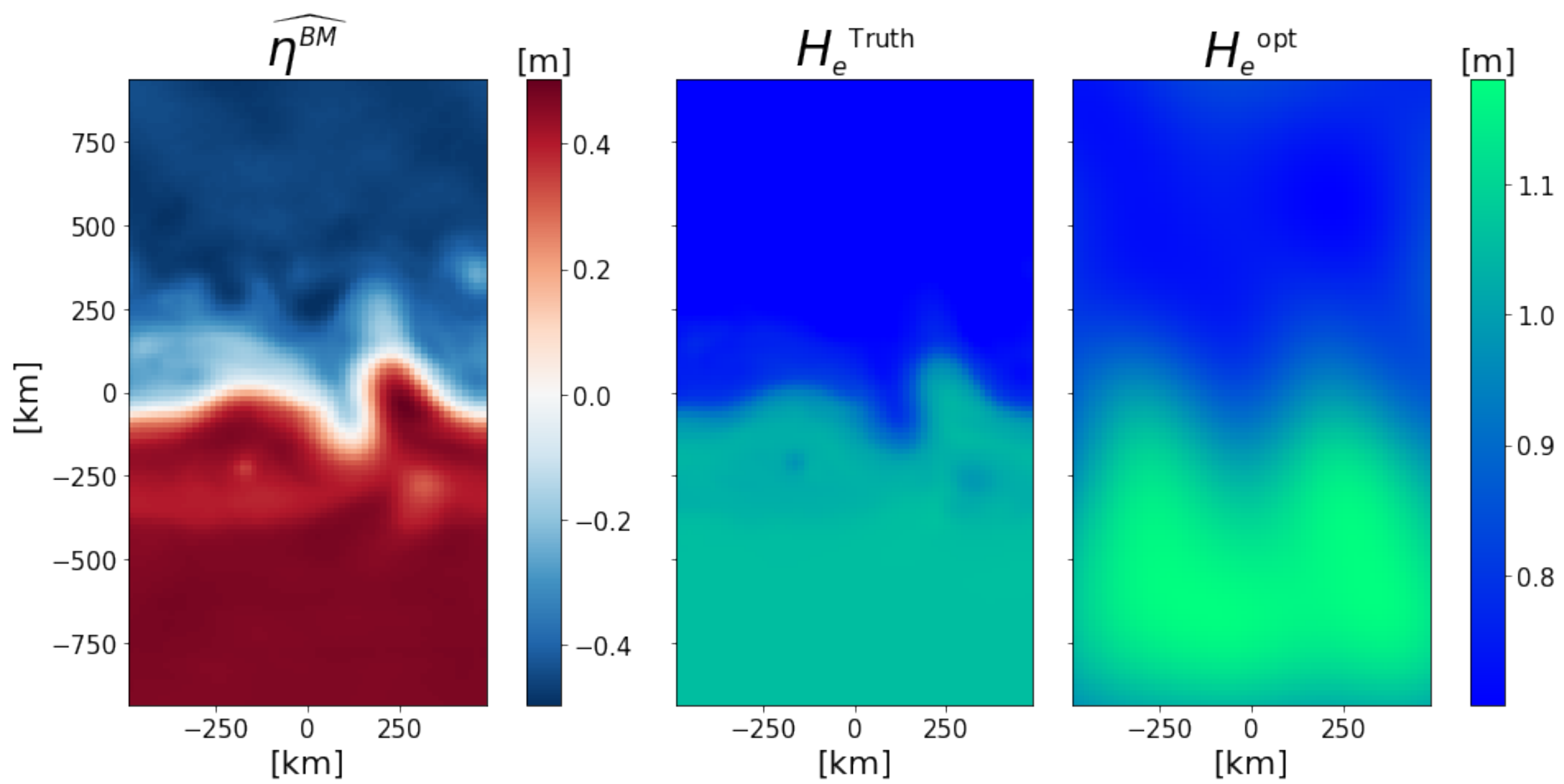
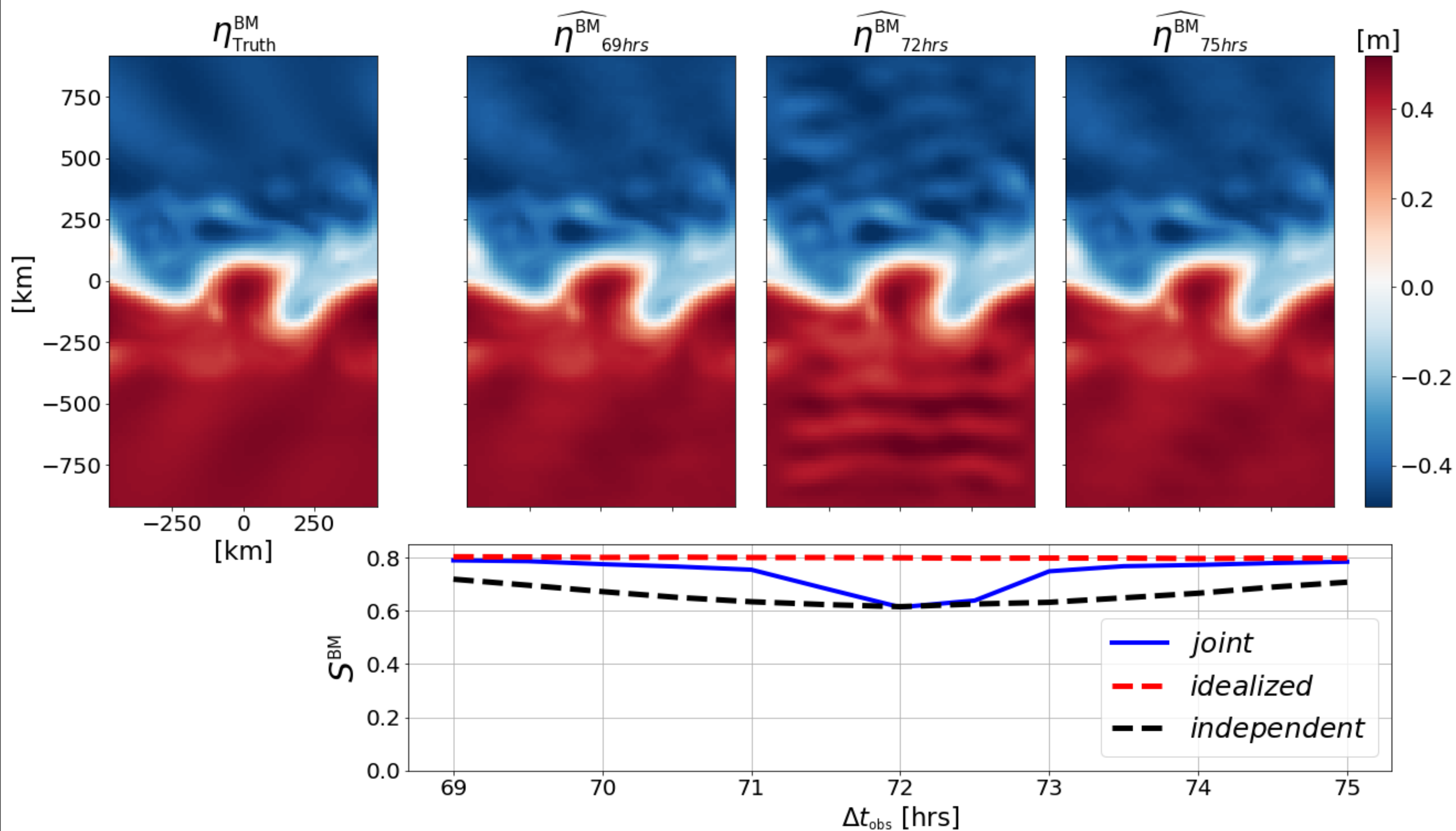


Figure 7.

Balanced motions



Internal tides

